A Mössbauer Study of Austenite Stability and Impact Fracture in Fe - 6 Ni Steel

By

Brent Thomas Fultz

B.S. (Massachusetts Institute of Technology) 1975

THESIS

Submitted in partial satisfaction of the requirements for the degree of

MASTER OF SCIENCE

in

Engineering Science

in the

GRADUATE DIVISION

of the

UNIVERSITY OF CALIFORNIA, BERKELEY

Approved:

.....

.....

.....

Committee in Charge

NOTICE

This report was prepared as an account of work sponsored by the United States Government. Neither the United States nor the United States Department of Energy, nor any of their employees, nor any of their contractors, subcontractors, or their employees, makes any warranty, express or implied, or assumes any legal liability or responsibility for the accuracy, completeness or usefulness of any information, apparatus, product or process disclosed, or represents that its use would not infringe privately owned rights.

.....

DISTRIBUTION OF THIS DOCUMENT IS UNLIMITED

TABLE OF CONTENTS

I. Introduction 1

II. General Theory of the Mössbauer Effect 4

III. Construction of a Mössbauer Spectrometer 8
- A. The Computer System
- B. The Source and Detector
- C. The Doppler Drive

IV. Experimental Procedure and Data Analysis 15
- A. The Experiments
- B. The Fe^{57} Nuclear Environment
- C. The Linear (Hyperfine) Perturbation Model
- D. Magnetic Considerations and the Austenite Equation
- E. Errors
- F. Implementation of Spectral Analysis

V. Experimental Results 28

VI. Discussion 30
- A. Austenite Stability
- B. Toughness

References

Tables

Figures

ACKNOWLEDGEMENT

This work was supported by the Division of Materials Sciences, Office of Basic Energy Sciences, U. S. Department of Energy.

A MÖSSBAUER STUDY OF AUSTENITE STABILITY AND IMPACT FRACTURE IN Fe-6Ni STEEL

Brent Thomas Fultz

Materials and Molecular Research Division, Lawrence Berkeley Laboratory
and Department of Materials Science and Mineral Engineering,
University of California, Berkeley, California 94720

ABSTRACT

The two phase ($\alpha + \gamma$) microstructure of a commercial cryogenic alloy steel was studied with regard to possible phase transformations induced by impact fracture. A backscatter Mössbauer spectrometer was constructed for measurements of atomic fractions of the two phases near specimen surfaces. Mössbauer spectra were collected from several types of unpolished and chemically polished surfaces of impact specimens to reveal (for the first time) the depth profile of the observed $\gamma \rightarrow \alpha'$ transformation near fracture surfaces. It was found that the spatial extent of transformation could be monotonically related to the impact energy absorbed by the specimen. These results are interpreted in light of several models of phase stability and impact toughness.

A general description of the Mössbauer effect and methods of spectral analysis is included. The method of linear perturbations in the hyperfine magnetic field is discussed with respect to its general usefulness in obtaining chemical information from Mössbauer spectra of the α phase. The procedure adopted for spectral analysis was chosen to provide an accurate phase analysis at the expense of chemical information. Both the Mössbauer equipment and analysis procedures were developed with the primary objective of providing a routine metallurgical phase analysis technique for low alloy steels.

I. INTRODUCTION

The scientific development of Fe-(5-12)%Ni steels for low temperature applications necessitates fundamental experimental studies of fracture effects in these alloys. There is currently much metallurgical interest in the importance of a second phase, austenite, which can be introduced into the primarily martensitic Fe-Ni microstructure.* The low temperature fracture toughness can be improved when austenite is present, but the beneficial role (if any) played by the austenite is unclear.

After a fine grained martensitic structure is tempered in the $\alpha + \gamma$ two phase region of the Fe-Ni equilibrium phase diagram (see Fig. 1), regions of reverted austenite are observable by transmission electron microscopy (TEM). From TEM micrographs [1,4,5,7-9] it is seen that the austenite reverted during two-phase tempering is formed as elongated regions along interlath boundaries and other internal surfaces of the martensitic structure. This morphology contrasts with the film-like austenite observed in alloy steels with higher carbon contents. [11] The amount of austenite formed during tempering can be determined by a suitable choice of tempering time. Many correlations have been drawn between the amount of austenite formed at lower tempering temperatures (~550°C) and the suppression of the ductile to brittle transition temperature (DBTT) for impact fracture in these alloys. [1-8] This improvement of low temperature ductility is not observed for higher tempering temperatures (>650°C) even though significant austenite volume fractions are readily obtained. This tempering temperature effect is only one indication that the volume fraction of austenite alone does not ensure a low DBTT. The enhancement of low temperature toughness found after a suitable tempering must be due to other, more subtle,

---

*Nomenclature for the two phases will be:
austenite ≡ γ phase (FCC structure)
martensite ≡ α phase (BCC structure)

microstructural characteristics of the austenite or perhaps due to changes in the martensitic structure as well.

Until recently, all quantitative correlations between toughness and the amount of reverted austenite in Fe-Ni steels have involved determination of the austenite volume fraction by diffraction methods. Unfortunately, TEM and x-ray diffraction techniques are of limited usefulness for irregular, plastically deformed fracture surfaces. However, quantitative data on the austenite content of a fracture surface is clearly needed in addition to austenite concentration information from the bulk of a specimen. This supplied the motivation for the development of a Mössbauer spectrometer system to study fracture surfaces directly.

As described in detail later, a Mössbauer spectrum is obtained by counting radiations from Fe^{57} nuclei in the specimen. Variations in the specimen crystal structures distinctly affect these nuclear spectra, and with some analytical effort it is possible to extract phase and chemical information from the spectra. The γ-rays used in Mössbauer spectroscopy cannot be focused; spectral information is averaged over a 0.1 - 1.0 cm^2 specimen surface area. The equipment to be described can provide austenite concentration information from shallow (<1000 Å) depths below the specimen surface. For fracture surface analysis Mössbauer spectroscopy is particularly valuable because it is not stymied by granularity, texture, or surface irregularities. Although subject to its own unique limitations, Mössbauer spectroscopy is a superior tool for quantitative phase analysis of fracture surfaces.

In addition to our alloy development interest in Fe-6Ni steel, there was an important ancillary reason for the study of this material. To our knowledge, the Fe-6Ni system is one of only two [7,9] alloy systems

whose fracture surfaces have been directly studied by TEM. Hiroyo Haga[7] obtained dark field micrographs of austenite in a specimen cut perpendicularly from an impact fracture surface. Haga observed austenite in close (~1μm) proximity to the fracture surface of an impact specimen which was intentionally designed for brittle fracture. This was interpreted as evidence that the good low temperature toughness of Fe-6Ni steel with the proprietary QLT treatment of the Nippon Steel Co. (see Fig. 1) was due to the mechanical stability of austenite against transformation to martensite, even when in the path of the fracture crack. The current Nippon Steel Co. Fe-6Ni QLT alloy steel was developed on the evidence that reverted austenite, mechanically stable during impact fracture, is a requirement for good low temperature toughness properties.

However, recent Mössbauer studies of Fe-9Ni [6,10], and now fracture profile TEM pictures of fracture surfaces in this alloy [9], have shown that reverted austenite near the crack path is not stable during impact or fracture toughness testing. In the light of the apparent conflict between Haga's Fe-6Ni work and the situation in Fe-9Ni steel, this study was undertaken to provide detailed data on the stability of reverted austenite in Fe-6Ni QLT steel.

In particular, embrittled specimens like those used by Haga were studied in order to assess possible discrepancies between austenite stability in these specimens and in standard Charpy specimens. The present study has served to reproduce the Fe-9Ni results for Fe-6Ni steel and has produced some new metallurgical data.

II. GENERAL THEORY OF THE MÖSSBAUER EFFECT

The Mössbauer effect was discovered and correctly interpreted by Rudolf Mössbauer in 1958. Since then, many good explanations of the effect have appeared in the hardcover and softcover literature.[15-18] In this section are presented brief descriptions of the basic features of the Mössbauer effect.

The Mössbauer effect involves two nuclei embedded in crystal lattices; one nucleus serves to emit a γ-ray as it decays from an excited state, and an absorber nucleus undergoes the reverse process. By the $\Delta E \Delta t \approx \hbar$ uncertainty principle, the relatively long-lived first excited state of Fe^{57} has sharply-defined energy (around 14.39 keV), so in order to excite this state by photon absorption, the energy of the incident photon must be within $\sim 10^{-8}$ eV of the mean state energy.

The existence of the Mössbauer effect depends on what happens to the recoil energy of the emitted γ-ray. Momentum conservation demands that the γ-ray recoil momentum ($\vec{P}_{recoil}$) is eventually taken up by the crystal of the radioactive source. The γ-ray emission process changes the nuclear part* (η_i) and may change the lattice part (α_i) of the initial state function for the system of nucleus and crystal, $|\alpha_i \eta_i\rangle$. By Fermi's second golden rule we can find the probability of a

---

*Notation for this section:

$\alpha \equiv$ set of lattice coordinates (i.e. nuclear centers of mass); usually normal coordinates.

$\eta \equiv$ set of internal nuclear coordinates.

Coordinate subscripts:

i ≡ initial	ex ≡ excited
f ≡ final	g ≡ ground

specific emission process:

$$P = (\text{const.})\ |\langle\alpha_f n_g|H_{cm}H_i|\alpha_i n_{ex}\rangle|^2$$

$$P = (\text{const.})\ |\langle\alpha_f|H_{cm}|\alpha_i\rangle|^2\ |\langle n_g|H_i|n_{ex}\rangle|^2 \qquad (1)$$

$H_{cm}H_i$ is the interaction hamiltonian associated with the nonzero vector potential (photon) at the nucleus. Since the internal nuclear coordinates and the lattice coordinates do not affect each other, their commutation allows us to separate the lattice and nuclear factors in Eq. (1). We need not consider $|\langle n_g|H_i|n_{ex}\rangle|^2$ to explain the existence of the Mössbauer effect, but perturbations in the nuclear levels contribute much information to Mössbauer spectra.

Without considering which phonon modes are excited or are excitable, we can see that there is something special about the $P_{ii} \sim |\langle\alpha_i|H_{cm}|\alpha_i\rangle|^2$ probability; it is associated with no change in phonon modes after a γ-ray emission. In this case, a small recoil energy, $\vec{P}^2_{recoil}/2nM$, is absorbed by all n nuclei (of mass M) in the lattice as a whole (and no energy is expended in heating the crystal). The emitted γ-ray hence escapes with virtually the full energy of the Fe^{57} excited state, and this energy is just the right amount (within $\sim 10^{-8}$ eV) to excite an Fe^{57} nucleus in the absorber crystal. This describes the process of recoilless emission, and occurs for certain nuclei in lattices when P_{ii} is significantly large.

The time dependence of the excited Fe^{57} nuclear state is exponential, so its precise energy distribution (the Fourier transform of $e^{-|t|/\tau}$) is a Lorentzian function $L_s \sim [1 + (\frac{E}{\hbar}\tau)^2]^{-1}$, where E is the difference from the mean nuclear state energy, τ is the state lifetime, and $\hbar$ is Planck's constant divided by 2π. This energy distribution is characteristic of the absorber nuclear states as well. However, in our absorbers (the steels) especially, there will be local environment

differences between Fe^{57} nuclei surrounded in different ways by neighboring atoms. A specific environment (the jth which is characteristic of a number, N_j, of Fe^{57} nuclei) will experience a perturbation of its nuclear states and will consequently center its Lorentzian lineshape about a shifted energy E_j so that:

$$L_{Aj}(E) = L_A(E-E_j) = \frac{1}{1+(\frac{E-E_j}{\hbar}\tau)^2}$$

Our Mössbauer spectra were obtained by scanning the emitted γ-ray energy through a small range by a first order Doppler shift which is proportional to the ratio of the velocity of the radioactive source to the speed of light, specifically $E_{Doppler} = \frac{V_{source}}{c} 14.4$ keV. For a particular V_{source}, the intensity of the Mössbauer effect (determined by counting radiations from the absorber) will be the convolution of the source and full absorber lineshapes; both a recoilless emission and a recoilless absorption must occur. Each local environment experienced by Fe^{57} nuclei will contribute to the full absorber lineshape its own Lorentzian absorption spectrum, L_{Aj}, weighted by N_j. The measured spectrum is hence:

$$S(V_{source}) \propto S(E) = \text{const.} \int_{-\infty}^{\infty} L_S(E'-E)\left\{\sum_j N_j L_A(E-E_j)\right\} dE'$$

In a more useful form:

$$S(E) = \text{const.} \sum_j N_j \left\{\int_{-\infty}^{\infty} L_S(E'-E)\, L_A(E-E_j) dE'\right\} \qquad (2)$$

The convolution of two Lorentzian functions is another (fatter) Lorentzian function. All Mössbauer spectra will hence have the form of a weighted sum of these fatter Lorentzians:

$$S(V_{source}) = K \sum_j N_j \frac{1}{1+k(E-E_j)^2} \qquad (3)$$

K, k are constants

The Fe^{57} first excited state has a spin of 3/2. In ferromagnetic α-Fe, there are found ($+\frac{3}{2}$, $+\frac{1}{2}$, $-\frac{1}{2}$, $-\frac{3}{2}$) orientations of this spin along the Fe hyperfine field which cause different perturbations of the first excited nuclear level. With two such orientations of the ground state spin of $\frac{1}{2}$, we observe a six line Mössbauer spectrum for a pure iron absorber (using our "single Lorentzian" source lineshape). The notation of Fig. 8 will be used for all references to each of the six individual peaks. No further perturbations (i.e. isomer shift or electric quadrupole splitting) affect the shapes or relative positions of the peaks in a pure iron spectrum. Section IV describes the effect of perturbing this six line spectrum with the presence of 3d impurity elements in the α-Fe lattice. Equation (3) will describe the observed spectrum, and the determination of N_j and E_j will be discussed.

III. CONSTRUCTION OF A MÖSSBAUER SPECTROMETER

The most important elements of the Mössbauer spectrometer used in this study are shown in Fig. 3. Much of the basic equipment operation will be described here, although it is well covered in the literature.[12, 15, 17, 19, 20] The source, detector, and specimen are within the lead box in the lower right of Fig. 3. The Doppler shift velocity of the radioactive source is provided in a cyclic manner (see Fig. 4) with a period of .16 seconds. During the first half-cycle the source undergoes a constant negative acceleration with respect to the stationary absorber, and the second half-cycle entails a positive acceleration of the same magnitude. The velocity hence varies linearly between $\pm V_{max}$ during each cycle. This cycle is divided into 512 equal time intervals. The number of detector pulses counted during each time interval are added to the previously collected counts from corresponding time intervals of previous cycles.

The equipment can be effectively classified into three subsystems: 1) the data collection and computer system, 2) the source and detector, and 3) the Doppler drive. The automatic operating mode of the spectrometer is characteristic of synchronized electronic systems, and the interrelationships of the three subsystems are best seen by reference to Fig. 4. 512 data service routines are performed every .16 seconds as the Doppler drive transducer completes each full cycle. High reliability of all equipment is necessary in order to allow operation on an almost continuous duty cycle (since 8-77).

A. The Computer System

Routine maniuplation of digital data is a task best performed by a small computer system, especially when the data consists of several hundred (512) discrete points. Our spectrometer was built around an 8

bit microcomputer with specialized hardware to enable operation as a data collection system. As desc bed in Ref. (12), the essential modification involved the design nd fabrication of circuitry to count detector pulses and synchronize the system timing. A block diagram of this scaling hardware is shown in Fig. 5. Even though the central processor service routine requires ∿60 μsec for each data counter, the use of twin time-multiplexed counters results in a mere ∿10 nsec dead time when multi-channel scaling.[12] The hardware and machine language software were optimized for the Z-80 microprocessor, which affords a high clock speed and an efficient data transfer instruction set.

Graphics hardcopy is provided to 1/60" x 1/48" resolution by a programmable flywheel printer. The unique interface logic needed to use this printer with our computer is shown in Fig. 5.* Experimental data, machine language codes, and data analysis programs in the language BASIC are all stored on floppy disks for convenient access. Certain primitive data manipulations (impossible with a multichannel analyzer) are routinely performed on all Mössbauer data.

Moving our radioactive source in a cyclic pattern gives two instants per cycle during which the source is stationary (at the nearest and furthest source-detector separations). About each zero velocity data channel will be a full Mössbauer spectrum, but the radiation intensity for the two spectra will not be the same due to the cycling source-detector separation. A parabolic distortion of the spectral baseline is hence quite visible in our raw data. "Folding" the data by adding together the data channels corresponding to the same source

*All custom hardware mentioned above were implemented with 65 integrated circuits on three 5" x 10" cards.

velocities will provide a first order correction to this distortion (in addition to doubling the effective count rate). For a source which travels maximum distances, ±d, from the mean source-detector separation, R, the folding process corrects the most distorted (i.e. zero velocity) count rates:

$$\frac{1}{(R+d)^2} + \frac{1}{(R-d)^2} \simeq \frac{1}{R^2}\left(1-2\frac{d}{R} + 3\left(\frac{d}{R}\right)^2 + \ldots\right) + \frac{1}{R^2}\left(1+2\frac{d}{R} + 3\left(\frac{d}{R}\right)^2 + \ldots\right)$$

$$\simeq \frac{1}{R^2}\left(1+6\left(\frac{d}{R}\right)^2\right) \cong \frac{1}{R^2}$$

Since $d/R \sim 0.01$, spectral folding provides an adequate correction for the parabolic baseline distortion (<5% error for our weakest spectra).

The inertia of the transducer causes the source motion to lag behind the synchronization signals from the computer. The center of folding turned out to be different from the center of the data by ~0.3 data channels, and this error would be expected to artificially broaden the folded lineshapes. Fortunately, spectra such as shown in Figs. 7-10, 14, 15 were not broadened by this amount. After folding, the spectrum was "compressed" whereby the contents of adjacent data channels were added together.* All spectra collected over a ±2.0 mm/sec Doppler range were compressed twice to enhance peak intensities and to reduce the folding error to $(1/2)^2$ (0.3) channels. After folding and twice compressing the data, only 64 independent data points were finally obtained from the original 512.

All programs and operating software described above were written directly in the Z-80 machine language code. However, any program requiring arithmetic operations more sophisticated than an addition (or not requiring high speed in data transfer) was written in the

*This is equivalent to counting twice as long at half the number of points in the Doppler cycle.

language BASIC developed for 8080 microprocessors using our floppy disk system. Control of data collection by subroutine calls from BASIC was implemented, and the computer was frequently used to run large calculational programs in BASIC in the 250 microsecond intervals between the service routine interrupts which handled the data collection (again see Fig. 4).

B. The Source and Detector

Fe^{57} nuclei in their first excited state are the result of an electron capture by Co^{57} nuclei. The Co^{57} atoms are dilutely diffused into a pure Pd matrix. The substitutional presence of Co^{57} is sufficiently low (especially for our source) such that the Fe^{57} nuclei "see" only Pd nearest neighbors. All Mössbauer spectra in this study were obtained with the naturally abundant Fe^{57} (2.2%) in our metallurgical specimens and with both source and absorbers at room temperature (although an effective Debye-Waller factor reduces the spectral intensity to one quarter of that for 0°K operation).

The source and detector are arranged for backscatter Mössbauer counting. Incident 14.4 keV γ-rays from the source pass through the detector with a low ionization probability of the light (96%He, 4%CH_4) detector gas. Our Mössbauer spectra were not collected by counting γ-rays emitted after recoilless absorptions in the source, but rather by counting internal conversion electrons which arise from processes in which the excited nuclear state energy is used to eject an electron from the metal. The mean free path of these <10 keV electrons is only a few hundred Å in steels.[21,22] Counting conversion electrons allows our Mössbauer spectrometer to perform as a surface (∿0.1μm) analytical instrument and concomitantly makes "thickness broadening" (due to

multiple Mössbauer processes) negligible in our spectra.[21,23]

Unfortunately, most of the source radiations do not give rise to recoilless processes, so Compton scattering and inner shell Auger processes contribute significant noise in the form of a high background count rate. These background counts completely determine the $\sim \frac{1}{\sqrt{N}}$ scatter of our Mössbauer spectra (i.e. N = background counts). A convenient figure of merit for our detector was the ratio of the total number of counts in a Mössbauer spectrum (experimental counts minus background counts) to the total number of background counts. This ratio, a mere $\sim 10^{-3}$ for a tantalum masked specimen surface, required $\sim 3 \times 10^{7}$ counts/channel (after folding and compressing) for good spectral resolution. With the source and specimen separated by 25mm, this required three or four days of counting for each specimen.

The distance of separation between the source and absorber surfaces, ℓ, calls for an engineering compromise. Point sources and absorbers would imply that all detected Mössbauer γ-rays travelled parallel to the vector $\vec{V}$ (transducer velocity vector). However, when source and detector diameters are significant, γ-rays not parallel to $\vec{V}$ will be counted. "Cosine broadening" of spectral lines and errors in line positions will result. Assuming an isotropic emission of γ-rays, an effective distribution of Doppler velocities (less than or equal to $\vec{V}$) can be calculated by analytical geometry. Numerical analysis of this problem for our source and detector diameters gives the result of Fig. 6. $P_{\ell}(\theta)$ is the geometrical probability of counting a γ-ray which traveled at an angle θ with respect to $\vec{V}$. The velocity error goes as 1-cos θ, so $P_{\ell}(1-\cos\theta)$ is the broadening function (which could be deconvoluted to yield a Mössbauer spectrum with no cosine broadening). Two source-detector

separations (ℓ = 48mm for $|\vec{V}|_{max}$ = ±6.7mm/sec, and ℓ = 25mm for $|\vec{V}|_{max}$ = ±2.0mm/sec) were used in this work.* These two separations result in acceptable spectral distortions without a deconvolution correction (see Fig. 6). Unfortunately, the maximum cosine broadening is associated with large specimen surface areas, small ℓ, and hence good data counting rates.

Our conversion electron proportional counter uses irregularly shaped specimen surfaces to seal the gas in its chamber while permitting a steady (~80 cc/min) flow of gas through the detector. This seal, partly molded of modeling clay, was a source of experimental difficulty. Fluctuations in the intensity of the ionization cascade were encountered with improper specimen-detector seals,** so it was often necessary to remount the specimen before starting data collection. The run to run variation of this seal made accurate calibration [21] of the single channel analyzer (SCA) window impossible, but fortunately this was not a critical adjustment. The SCA window settings were performed with skilled observations of the detector pulses on an oscilloscope.

C. The Doppler Drive

The motion of the radioactive source was achieved with a commercial (Austin Science Assoc. S-600) electromagnetic drive system. The most significant bit of the binary address counter (see Fig. 5) is a square wave in time. The Doppler drive electronics integrates this signal to generate an accurate triangle wave which is used as a reference signal. A coil in the transducer serves to generate a voltage proportional

*Fortunately for minimum cosine broadening, most of the usable specimen surface areas were small enough to give narrower $P_\ell(\theta)$ functions than those of Fig. 7.

**Grounding problems were also responsible for changes in ionization amplification.

to its velocity as it moves in a steady magnetic field. The difference between this velocity waveform and the reference signal is used to drive the main power coil of the transducer so that the transducer velocity is linear in time, just like the reference signal. This linearity was checked by triggering an oscilloscope on changes of the second most significant bit in the address counter of Fig. 5 (the transducer should be nearly at rest at that instant). The drive motion was linear to at least 0.5%. Approximately two pure iron samples were run each month to check the stability of the drive system. No long term drift (i.e. <0.2%) was ever observed. This is of extreme importance when making quantitative comparisons of different spectra, as described in the next section.

IV. EXPERIMENTAL PROCEDURE AND DATA ANALYSIS

A. The Experiments

Fe-6Ni-1Mn steel plate was received from the Nippon Steel Co. with the commercial QLT heat treatment after rolling (see Fig. 1 for composition and temperatures). Impact specimens were cut parallel to the rolling direction of the plate and were prepared for fracture as: 1) standard Charpy specimens, 2) fatigue precracked Charpy specimens, and 3) constrained-fatigue-notched (CFN) specimens as described by Haga and shown in Fig. 2. Charpy energies were in good agreement with Japanese data for this steel [5,7], although only two Charpy specimens were broken at both 77°K and 298°K temperatures. The fractured specimens were stored in a $CaCl_2$ dessicator until the time of their Mössbauer run. Fracture surface shear lips, fatigue cracked surface, and machined areas of the impact specimens were not examined by the detector. Much of a specimen fracture surface was shielded from conversion electron penetration by specially fit pieces of .01" tantalum sheet held together by modeling clay.

The radioactive Co^{57} in Pd source had decayed to 10 mCi by the time of these experiments. In addition, the small usable specimen surface area ($<0.5\ cm^2$) and the poor recoilless counting efficiency of the backscatter electron proportional counter necessitated careful compromises (described in Sections III and IV) in order to accumulate good data for a specimen in only three days. By adjustment of the proportional counter and the SCA, conversion electron energies were chosen such that electrons originating within $\sim 0.1\mu m$ of the surface of the steel were counted.

In order to determine the distribution of austenite below the fracture surfaces, three specimen surface preparations were used in this study.

Fracture surfaces were analyzed in: 1) the as-broken condition, 2) after ~0.01cm removal of material , and 3) after ~0.1cm removal of material. The polishing procedures are shown in Table II. Specimens in a set for comparison were acid polished simultaneously in the same solution. Consistency in the depth of polishing was determined by optical microscopy, but a possible error of a factor of two in the absolute depth of polishing made this the least accurate part of this study. A fracture surface does not polish evenly.

Independent experimental confirmation of the (volume) fraction of austenite was provided by CuK_{α} x-ray diffraction. The austenite analysis technique of Miller [13] was found useful for polished regions of undeformed material.

In addition to its data collection role, the Z-80 system performed all numerical calculations needed for data analysis in this study. Computations were time-shared with data collection when they required more than ten hours of microprocessor time.

B. <u>The Fe^{57} Nuclear Environment</u>

In the next few pages we will apply Eq. (3) to spectra from Fe-6Ni steel in quest of metallurgically useful information. The experimental spectra will be analyzed as weighted sums of Lorentzian functions with equivalent linewidths but different mean energies. There will in general be a different Lorentzian function for each nuclear environment (indexed by "j") experienced by an Fe^{57} nucleus with a probability P_j. Such a sum of Lorentzian functions can no longer be described by a Lorentzian $\sim[1 + (x)^2]^{-1}$ functional form, and deviations from this form can provide phase and chemical information.

An important such deviation for Fe-6Ni martensite is caused by the

perturbation of the Fe^{57} hyperfine field with the substitutional presence of Ni atoms in the α-Fe lattice. Good calculations of the magnitude of this effect are not possible by first principles alone.[24] Empirically guided first principles considerations[25-29] show that multiple spin polarization effects are the cause of these hyperfine field changes. The rather localized 3d electrons are responsible for the Fe^{57} hyperfine field in that they polarize the s electrons near the nuclei. The presence of a 3d transition metal impurity atom in the α-Fe lattice will hence alter this polarization at nuclei near the impurity atom. The (4s-like) conduction electron polarization is believed to be less important in Fe-Ni alloys because only a small term expressing direct proportionality between Ni concentration and hyperfine field is necessary to account for the observed Mössbauer spectra.[30]

It was rather beyond the scope of this work to study mechanisms of spin density oscillations around impurity atoms. Clearly no small amount of work is needed before these fundamental mechanisms can be used in practical, routine spectral analysis procedures (especially for significant Ni contents).

C. <u>The Linear (Hyperfine) Perturbation Model</u>

A phenomenological linear hyperfine perturbation model was described by Wertheim et al.[30] in 1964. The presence of a Ni atom in one of the nearest-neighbor (n.n.) shells of an Fe^{57} nucleus is assumed to perturb the hyperfine field by a constant amount characteristic of that shell. A convenient notation which describes the presence of Ni atoms in the nearest neighbor shells of an Fe^{57} nucleus uses a vector $\underset{\sim}{n} = (a,b,c,d,..)$. This particular Fe^{57} nucleus has a Ni atoms as first n.n.'s, b Ni atoms as second n.n.'s, c Ni atoms as third n.n.'s, etc. In the linear

perturbation model we assume that the Ni occupancy described by $\underset{\sim}{n}$ = (0,x,0,0,0...) will perturb the hyperfine field x times as much as will the arrangement $\underset{\sim}{n}$ = (0,1,0,0,0...). Note that the direction of the hyperfine field is ignored; we have not yet considered anisotropic effects. With the shift associated with each shell also expressed in the form of a vector $\underset{\sim}{h}$ = ($\Delta h_1, \Delta h_2, \Delta h_3, \Delta h_4$...), the spectral peak position for all nuclei with a specific $\underset{\sim}{n}_j$ is just $E_j = E^\circ (1 + \underset{\sim}{h} \cdot \underset{\sim}{n}_j)$, where E° is the distance of the pure Fe unperturbed peak from the center of symmetry of the pure Fe 6 line spectrum. It is proportional to the α-Fe hyperfine field times a constant spin and gyromagnetic factor.

We expect the probability of n_i atoms in the $i^{\underline{th}}$ n.n. shell to be the binomial probability function, $P(n_i, C_{Ni}, l_i)$, where C_{Ni} is the atomic fraction of Ni and l_i is the number of lattice sites in the shell.* The probability of a full configuration $\underset{\sim}{n}_j$ of shell occupancies is the product of the P's for the individual shells. This probability distribution will be exactly true for a truly random Fe-Ni substitutional solid solution. The final Mössbauer spectrum will be the sum of Lorentzian curves,** each characteristic of a different $\underset{\sim}{n}_j$ and weighted by the net binomial probability for the $\underset{\sim}{n}_j$ (the product of individual shell binomial

---

* This is like the probability of throwing n_i nickel atoms into the $i^{\underline{th}}$ n.n. shell with $C_{Ni} \sim$ the probability of success per throw, and $l_i \sim$ number of throws.

** Included with $\underset{\sim}{h} \cdot \underset{\sim}{n}$ in the denominator could be also a term $\underset{\sim}{j} \cdot \underset{\sim}{n}$, where $\underset{\sim}{j}$ is a set of isomer shift parameters. For the M6 peak to be described however, we can neglect isomer shift contributions since $E^\circ(\underset{\sim}{h} \cdot \underset{\sim}{n}) >> \underset{\sim}{j} \cdot \underset{\sim}{n}$. There was no observable electric quadrupole splitting in the Fe-6Ni martensite spectrum either, in agreement with Vincze and Campbell. 34

probabilities):

$$S(E) = K \sum_{\{\underline{n}_j\}} \frac{1}{1+k(E-E^{\circ}(1+\underline{h}\cdot\underline{n}_j))^2} \prod_{i=1}^{\text{n.n. shells considered}} P(n_i, C_{Ni}, l_i) \qquad (4)$$

The set $\{\underline{n}_j\}$ ranges over all n.n. shell Ni configurations consistent with the BCC structure. Mössbauer analysis techniques have also been refined to subclassify the n configurations by their symmetry with respect to the Fe^{57} principal quantization axis (i.e. hyperfine field direction).[31-33] At least one more parameter per n.n. shell is required in order to include these anisotropic effects in Eq. (4), and the number of terms in this sum becomes geometrically greater.

As the number of parameters for this linear model increases, a greater flexibility in approximating an arbitrary function is developed. The difference between calculation and experiment can be made smaller by optimum choices of parameters, but with the scatter of the data (especially as in this study) it soon becomes clear that strikingly different choices of parameters result in good fits to experimental spectra. This problem with the effective non-uniqueness* of hyperfine parameters is a major limitation of Mössbauer spectroscopy for local chemical analysis. The difficulties with Fe-Ni alloys are less severe with Fe-Cr [30, 31, 34, 35] and other alloy systems where the Δh_i's are several times larger. An exciting Mössbauer study of the Fe-Cr-Co system (which used a form of Eq. (4)) has been effective in showing the local changes of composition associated with spinodal decomposition in this system.[36]

*For instance, compare the hyperfine parameters found in Refs. 28 and 32 for Ni in α-Fe.

A one parameter adaptation of Eq. (4) was used to fit the lineshapes of Fe-6Ni steel.* Careful experiments by Vincze and Campbell [34] show that $\Delta h_1 \approx \Delta h_2$ for Ni atoms in α-Fe. (We naïvely note that BCC second nearest neighbors are only 1.15 times as far away as first nearest neighbors and are not geometrically occluded by spheres centered at first nearest neighbor sites.) In the popular two shell isotropic treatment Eq. (4) becomes:

$$S(E) = K \sum_{i=0}^{8} \sum_{j=0}^{6} \frac{1}{1+k[E-E^{\circ}(1+\Delta h_1 i+\Delta h_2 j)]^2} \binom{8}{i} C^i (1-C)^{8-i} \binom{6}{j} C^j (1-C)^{6-j} \qquad (5)$$

$$C \equiv \text{atomic fraction Ni}$$

The reduced specificity of setting $\Delta h_1 = \Delta h_2 \equiv \Delta h$ leads to a significant simplification of Eq. (5). We note that $\Delta h_1 i + \Delta h_2 j = \Delta h(i+j)$ and define $s \equiv i+j$. With the addition theorem for binomial coefficients,

$$\sum_{i=0}^{8} \sum_{j=s-i}^{6} \binom{8}{i} \binom{6}{j} = \sum_{s=0}^{14} \binom{14}{s} \quad ,$$

we obtain:

$$S(E) = K \sum_{s=0}^{14} \frac{1}{1+k[E-E^{\circ}(1+\Delta hs)]^2} \binom{14}{s} C^s (1-C)^{14-s} \quad .$$

An effective 14 nearest neighbor shell model is now considered.

k was determined from the linewidth of the α-Fe spectrum, which is shown to be a good Lorentzian in Fig. 7. The unperturbed positions of the M1 - M6 peaks were taken to be those of pure Fe (Fig.7). Δh and

---

* Sophistication was limited by the data quality.

C were left as parameters in the program for the calculation of S(E) from Eq. (6). The minimum RMS error between this S(E) and the full Fe-6Ni martensite spectrum was found for Δh = 2.8%/Ni atom when C = 5.5 A/o Ni, in good agreement with Vincze and Campbell.[34] For these parameters an enlargement of the M6 peak is shown in Fig. 10a. The lack of fine structure in the experimental data is attributed to further nearest neighbors, impurities other than Ni, and, of course, data scatter. Increasing the component linewidth ($\sim \frac{1}{\sqrt{k}}$) by 30% gave the result shown in Fig. 10b.

As in previous work with this 14 atom shell model and our experimental data[35], good fits for other values of C were possible with a suitable adjustment of Δh. As a rule of thumb, good fits are obtained whenever $C \cdot \Delta h \approx 15$ (A/o Ni)(%/Ni atom). Nevertheless, for a predetermined Δh, fitting Eq. (6) to the data will give a unique C. (For instance, with Δh = 2.8%/(Ni atom)we can say that C = 5.5±1A/o Ni for a spectrum collected in ∿1 week with the equipment used in this study). A serious attempt to determine the usefulness of the linear hyperfine perturbation model for determining the Ni content of martensite was not made. Such a study would, of course, examine a variety of Fe-Ni compositions for a good test of several different shell models.

The parameters giving the best fit of Eq. (6) to the Fe-6Ni martensite spectrum give only a very small distortion (broadening ∿.5 channels) of the M3 and M4 peaks. This is observed experimentally in Fig. 9 An isomer shift effect towards positive Doppler velocities is also seen in these peaks. This isomer shift is in the same direction as the hyperfine perturbation shift for the M4 peak[34, 37-39], but will tend to counteract the hyperfine broadening shifts of the M3 peak. The

full width at half maximum of M4 is hence $\sim 3\times10^{-2}$ mm/sec larger than that for M3.

As will now be shown, when the linearly perturbed peak width is only slightly ($\lesssim$10%) greater than that of the unperturbed Lorentzian, an excellent approximation to the new lineshape can be achieved with a single Lorentzian curve. Single Lorentzian functions were fit numerically to the lineshapes generated with Eq. (6) using C_{Ni} = 0.055 and a set of 20 Δh's. The best fit was found by the minimum RMS error between the two functions, and the absolute area error (the total area lying between the two curves) was also computed. The results, shown in Fig. 11 and 12 show that the absolute area error is quite small for our predicted M3 and M4 peaks (Δh = 2.8%/Ni atom, C_{Ni} = 0.055 gave $j/J \sim .9$), approximately only 2%. This result is disheartening from the chemical information point of view; nearest neighbor information is best obtained when a peak has an unusual, non-Lorentzian shape. However, as utilized in Section IV.F. for phase analysis, the single Lorentzian approximation for M3 and M4 is a great convenience.

D. Magnetic Considerations and the Austenite Equation

The energy range scanned in our Mössbauer spectra was made small so that as much counting time as possible would be devoted to the austenite peak. This was necessary for efficiency in data collection, but it made some other general features of the martensite spectra necessary for spectral interpretation. It is immediately obvious from Fig. 8 that the M1-M6 peaks do not have the 3:2:1:1:2:3 intensity ratio predicted for a random, polycrystalline absorber.[40-41] The integrated intensity ratios of peaks M1-M6, 3.0:2.6:1.0:1.0:2.6:3.0, were characteristic of all full martensite spectra from fracture surfaces

in this study, and indicate a modest tendency for magnetization directions to lie parallel to the surface of the specimen.[40,41]

Subject to the errors to be described shortly, the atomic fraction of austenite (γ-phase) is equal to the ratio of the paramagnetic austenite peak area to the full Mössbauer spectrum peak area (i.e. net area of austenite peak + M1 +M2 +...+M6). However, our spectra were only collected over a $V_{max} = \pm 2.0$ mm/sec velocity range and do not include the M1, M2, M5, or M6 peaks. Nevertheless, with the martensite peak intensity ratios of the previous paragraph we need only relate the intensity of the austenite peak to M3 and M4 in order to determine the atomic fraction of austenite:

$$A/o\ \gamma = \frac{\text{Area } \gamma}{\text{Area M3 + Area M4}} \cdot \frac{1}{(3.0 + 2.6 + 1.0)} \cdot 100\% \qquad (7)$$

The polished surfaces showed variations in the intensity ratios of M1-M6, but resultant errors in using Eq. (7) directly were always less than $(0.1) \cdot (A/o\ \gamma)$. Equation 7 is an adaptation of the "seven peak approximation" first used by Marcus et al.[42] and described by others for several steels.[43-45]

E. Errors

Implicit in Eq. (7) is the assumption that the recoil-free fractions of Fe^{57} in austenite and Fe^{57} in martensite are the same. Differences between BCC and FCC phonon spectra will hence make the determination of austenite concentration somewhat in error. From crude predictions of the Debye model we can estimate the recoil-free fraction difference. The Debye temperature, θ_D, of pure α-Fe is $\sim$420°K.[46,47] With specific heat data, Y. Tanji[47] has determined θ_D for FCC Fe-Ni alloys of most compositions. θ_D was found to vary ±15°K around 450°K. Our worst error (assuming an arbitrary Ni content in the austenite) due to the

assumption of equal recoil-free fractions is hence proportional to $e^{-300/465} - e^{-300/435}$ and is determined to be ∿5% of the atomic fraction of austenite.

If the austenite Ni concentration is higher than that of the martensite, an obvious dilution of Fe^{57} error will be incurred. A Mössbauer study of carbon steel by Kim and Schwartz [48] showed that a more subtle problem exists with surface measurements of retained austenite. They found that the strain energy boundary condition of a nearby free surface causes some transformation of austenite to a depth of 1-10μm. This effect gave a ∿20% change of the less stable austenite in commercial 1095 carbon steel. The good agreement between Mössbauer and x-ray diffraction austenite determinations for polished surfaces indicates that reverted austenite in Fe-6Ni steel does not undergo a significant surface transformation; the depths characteristic of these two techniques are quite different. Fortunately, surface transformation and also the small anticipated errors of dilution and recoil-free fraction differences are not expected to significantly distort the ratio of austenite concentration in one specimen to that in another.

Equation (7) also assumes a complete correspondence between crystal structure and the presence of a nuclear hyperfine field. The hyperfine field, however, will not necessarily differ from its bulk FCC or BCC values only in the small region of the crystal interface (∿10 Å) between austenite and martensite. Errors in Eq. (7) could conceivably be due to either: a) Fe^{57} nuclei in austenite experiencing a nonzero hyperfine field, or b) Fe^{57} nuclei in martensite exhibiting less than the bulk hyperfine field. Both of these interface problems would be expected to get worse with decreasing grain size. Fortunately, the good agreement

between x-ray and Mössbauer analysis of austenite in grain refined Fe-9Ni steel [10] seems to indicate a narrow hyperfine field transition region between the two phases. Thin film Mössbauer experiments by Varma and Hoffman [49] showed the presence of a nearly full (~300 kOe) hyperfine field for films thicker than ~7Å. If we assume a proportionality between lattice and hyperfine magnetic fields, these thin film experiments are in good agreement with iterative magnetization calculations by Pearson. [50] His calculations also predict a very thin transition region (~10 atoms) for magnetization near a crystal surface. Those few martensite nuclei in this transition region would be expected to contribute to a diffuse (apparently undetectable) spectral background at the expense of the six line martensite spectrum.

Since the penetration of incident γ-rays into the specimens is about two orders of magnitude deeper than the region from which detectable conversion electrons originate, we need not consider intensity loss differences of the incident radiation in the two phases. However, it is not easy to estimate the error due to differences in energy losses when electrons pass through equal volumes of the two different phases. (Naively we expect that the conversion electron mean free path would be similar in both phases since their densities and chemistries are not particularly different). Again, perhaps the best indication that this source of error is not serious is the comparison of data between x-ray diffraction and Mössbauer phase analyses of undeformed, polished surfaces. The two techniques agree within the ±2-3 A/o accuracy characteristic of x-ray diffraction and the Mössbauer data is more reproducible.

Practical experience and overall consideration of the sources of error in Mössbauer austenite analysis indicate that the accuracy of this

technique is quite good. For austenite concentrations of 0-10 A/o it is estimated that an accuracy as good as ±1/2 A/o is possible and an accuracy of ±1 A/o is likely.

F. Implementation of Spectral Analysis

The Mössbauer spectra in this study consisted of contributions from three phases whose parameters are listed in Table I. In the course of this work austenite and martensite were readily identified, but a weak doublet peak identified as β-FeOOH [51-53] was also observed. This corrosion product was difficult to avoid in experimental practice, and unfortunately its two peak centers lie very close to the centers (i.e. less than the linewidths) of the M4 peak and the austenite peak. The sum of two Lorentzian curves of the same linewidth and the same energy is another Lorentzian of the same parameters, and cannot be decomposed uniquely into two component curves. However, even in the case of complete overlap of the β-FeOOH peaks with the M4 and austenite peaks, the doublet lineshapes allow a unique decomposition of our spectra.

Consider the case of complete overlap as shown schematically in Fig. 13. We can obtain the three intensities I_1, I_2, and I_3, and also know that the intensities of both peaks in our doublets are equal. With five linear independent equations and with the five component peak intensities as unknowns, we can always get a unique ratio of Area γ/(Area M3 + Area M4) for use in Eq. (7). The determination of I_1, I_2, and I_3 must consider the overlapping tails of the spectral peaks, however.

In practice the Mössbauer spectra were decomposed digitally. We know (see Figs. 9, 11) that the M3 and M4 lineshapes are closely Lorentzian. Hence Lorentzian curves for M3 and M4 were subtracted from the data giving a maximum possible area error in the remaining

spectrum of less than 0.05 times (Area M3 + M4). These two "stripped" peaks had identical areas, but the linewidths and centers were those of Table I. Since the M3 peak is not coincident with peaks from either β-FeOOH or austenite, the area* of these two stripped functions was determined to be that required to give a "flat" baseline near the previous maximum of M3.

With the use of this two peak stripping technique, a possible pitfall in the austenite analysis of Fe-6Ni steel can be avoided. Fig. 14 shows a distinct peak between the M3 and M4 peaks, which might nāively be interpreted as evidence of ∿2 A/o austenite. With the stripping of M3 and M4 as described, however, we find that this polished Charpy fracture surface contains less than 1/2 A/o austenite. The possible austenite peak in the experimental data was found to be half of a β-FeOOH doublet. Further stripping of the remaining spectrum was occasionally necessary in order to determine Area γ for Eq. (7).

It should be mentioned here that the stripping of an experimentally obtained pure martensite spectrum from the raw data shown in Fig. 14 was also performed. This procedure gave the same β-FeOOH doublet result, but the scatter in the stripped spectrum was noticibly worse. A very clean (long accumulation time) and pure (no rust) martensite spectrum is necessary for this stripping procedure, so for time efficiency in data collection the pure Lorentzian stripping technique is preferred. Stripping out the β-FeOOH or austenite peaks was also occasionally necessary, and pure experimental spectra of these phases were unobtainable.

The austenite peak (see, for example Fig. 15) in all spectra was somewhat broader than the M3 and M4 lineshapes. This broadening may be

*This was used directly in Eq. (7) to give [Area M3 + Area M4]$^{-1}$.

due to isomer shifts associated with different Ni nearest neighbor configurations. The broadening would occur analogously to the hyperfine broadening described by Eqs. (4-6), but with an $\underset{\sim}{j}\cdot\underset{\sim}{n}$ (instead of $\underset{\sim}{h}\cdot\underset{\sim}{n}$) type of line shift. With the improper use of Ni in α-Fe isomer shift data, the observed broadening would imply a distribution of Ni contents in the austenite of up to ∿30 A/o Ni. However, electric quadrupole and weak magnetic effects may also cause this broadening. The importance of these effects might be determined by taking a Mössbauer spectrum when a saturating magnetic field is applied perpendicularly to the γ-ray direction; resulting line shape changes will not be due to the isomer shift. This experiment may also give information on the correspondence between phase and the presence of a hyperfine magnetic field.

V. EXPERIMENTAL RESULTS

No austenite was ever observed (0.0 ± 0.5 A/o) on any fresh impact fracture surface of Fe-6Ni QLT steel. Clearly, the presence of austenite at a fracture surface cannot be correlated to ductility because austenite in the immediate vicinity (<0.1 μm) of a fracture surface always undergoes a >95% transformation to martensite.

A deeper study shows an increasing presence of austenite with depth below the fracture surfaces. These depth profile results (see Fig. 16) show how the (spatial) extent of the $\gamma \rightarrow \alpha'$ transformation* is dependent on specimen geometry and impact testing temperature. Specimens with the same geometry (either Charpy or CFN) exhibit a more extensive transformation at room temperature than at 77°K, and specimens of the Charpy geometry exhibit a more extensive transformation than CFN specimens at either temperature.

With the definition of a characteristic depth as the distance below the fracture surface where half of the reverted austenite has transformed, the relationship between absorbed impact energy and the characteristic depth of transformation is shown in Fig. 17. Close examination of the fracture profile TEM micrographs of Haga[7] indicates an increasing presence of austenite with depth away from his fracture surfaces. With a characteristic depth of 1-10 μm, Haga's specimen (6 ft·lb)** is indicated with an "x" on Fig. 17 and appears consistent with the data of this work. The smooth shape of this graph must be interpreted with caution; the accuracy of the depth axis is directly dependent on the accuracy of

---

* The prime (') indicates no composition change in this transformation.

** This low value is attributable in part to his high temperature austenitizing.

chemical polishing. However, specimens of the same geometry, which had similarly irregular fracture surfaces when examined optically, would be expected to exhibit similar chemical polishing characteristics. It is hence reasonable to assume that relative comparisons of depth profile data for specimens of the same geometry (but different testing temperatures) are inherently more accurate than the general comparison of all points of Fig. 17. Nevertheless, the data of Fig. 17 give strong indication that the depth of the $\gamma \rightarrow \alpha'$ transformation is dependent on the specimen geometry and temperature factors only in that they determine the absorbed impact energy. Perhaps this is evidence of an empirical rule for austenite stability during impact fracture in Fe-6Ni QLT steel.

Fig. 18 combines the information of Figs. 16 and 17 to show the extent of transformation of the reverted austenite as a function of impact energy. The quantity used for the z-axis is the fraction of reverted austenite which had transformed to martensite.

VI. DISCUSSION

A. Austenite Stability

The reverted austenite which is present in Fe-6Ni QLT steel at room temperature also is thermally stable at 77°K; the amount of austenite in undeformed polished surfaces of both 77°K and 298°K impact specimens was found to be 10.5 ± 0.5 A/o. Lower temperatures must be achieved in order to determine the $\gamma \rightarrow \alpha'$ transformation completion temperature (M_f), if such a temperature exists.

On the other hand, the temperature below which the $\gamma \rightarrow \alpha'$ transformation may occur under stain (M_d) lies above room temperature. Hence at both impact testing temperatures there was a thermodynamic driving force for the formation of martensite, and this free energy difference was presumably larger at 77°K than at 298°K. However, we can rule out the possibility that this thermal dependence of the $\gamma \rightarrow \alpha'$ free energy difference alone is what dominates the $\gamma \rightarrow \alpha'$ transformation. In particular, the extent of the transformation (Figs. 16 and 17) is less at 77°K than at 298°K, which is the reverse of predictions based only on a thermal driving force. In addition, the $\gamma \rightarrow \alpha'$ transformation does not occur unless there is a change in the stress or strain distribution in the microstructure.

Two roles of the strain energy in the $\gamma \rightarrow \alpha'$ transformation are envisioned which are compatible with the data of this study. The two roles differ in fundamental assumptions of austenite stability, but are not necessarily mutually exclusive. If the $\gamma \rightarrow \alpha'$ free energy difference were not significantly affected by changes in the microstructural strain distribution, then the role of the strain energy would be limited to introducing nuclei in the austenite needed before the thermal dependence of the free energy could force the $\gamma \rightarrow \alpha'$ transformation. These nuclei

would consist of suitable dislocation configurations (since the $\gamma \rightarrow \alpha'$ transformation occurs by shear) which would be developed during plastic deformation of the austenite crystals. If this nucleation problem dominated the kinetics of the $\gamma \rightarrow \alpha'$ transformation, one would expect this transformation to occur only within the plastic zone of the fracture surface. This is consistent with the extent of transformation seen in Figs. 16-18 when one assumes that the absorbed impact energy and plastic zone size are directly related.* This nucleation-dominated model is also in agreement with the well known tendency of austenite to be stabilized by its presence as small particles [54] (in which a nucleus is less likely to exist). This $\gamma \rightarrow \alpha'$ transformation model leaves little room for the importance of thermal or mechanical instabilities of the austenite, however. The existence of an M_f, for instance, would mean that thermal driving forces can overcome the nucleation barrier, and may thus imply a less extensive transformation at 298°K than at 77°K.

The second role of the strain energy gives it a more direct importance in the $\gamma \rightarrow \alpha'$ transformation. If the free energy difference for the transformation were strongly dependent on the local stresses in the austenite, then we can develop a qualitative explanation for the behavior of reverted austenite during impact fracture with a simple picture of austenite islands stabilized by local stresses from the surrounding martensite. (Compressive stresses would be expected to stabilize the dense FCC phase). When a re[illegible]aterial undergoes plastic flow, these local stress fields change their magnitudes and directions (and tend to be tensile in character near the crack tip). This picture predicts that the austenite will transform in response to some intensity of plastic

* This assumption seemed reasonable on optical examination of the fracture surfaces and can be supported by phenomenological metallurgical arguments.

flow which spoils the local strain criteria necessary for its existence. The depth away from the fracture surface where the strain changes are sufficient to transform a specific fraction of austenite would be expected to depend on the extent of plastic deformation, and as in the previous role model the $\gamma \rightarrow \alpha'$ transformation would be expected to occur within the plastic zone of the fracture surface.

Although the present study was able to determine the extent of the $\gamma \rightarrow \alpha'$ transformation as a function of temperature and strain energy (or rather a less precise impact energy), only the single composition and heat treatment of Fig. 1 was used in this work. Consequently, the importance of the nickel content in influencing the austenite stability could not be directly determined. The 600°C tempering part of the QLT treatment would produce austenite with a composition of somewhat less than 20% Ni, according to the Fe-Ni equilibrium phase diagram. The observed thermal stability of the reverted austenite may be due in a large part to this higher Ni content.

B. Toughness

A clear conclusion which may be drawn from the data of Figs. 16-18 is that the stability of austenite against the $\gamma \rightarrow \alpha'$ transformation during fracture is not the cause of the low DBTT of Fe-6Ni QLT steel. The large extent of this transformation concomitant with ductile fracture indicates that the austenite lying in advance of the crack tip transforms after plastic deformation has begun around it. This rather passive behavior of the reverted austenite is inconsistent with many models developed to relate the presence of reverted austenite to good cryogenic toughness properties. Models which involve the dynamics of interaction between the crack tip and a ductile austenite particle are incompatible with the above picture since there would be only α and α' martensite at

the crack tip. In particular, any model which relies on the stability of austenite against transformation while its twelve slip systems blunt the crack is clearly inconsistent with the data of this study.

Transformation induced plasticity (TRIP) toughening would predict a more extensive $\gamma \rightarrow \alpha'$ transformation in specimens which had undergone a more ductile fracture, in agreement with the present data. Unfortunately, stress times dilatation arguments predict negligible energies for the small volume fraction of austenite which transforms. The $\gamma \rightarrow \alpha'$ transformation is thermodynamically downhill, and it is difficult to see how it could absorb strain energy other than by considering these impotent force times distance arguments. The transformation would be expected to evolve heat, however. A 2 eV per atom free energy decrease after the austenite transforms would imply that the austenite transformation in the plastic zone would raise the local temperature by over 100°C (presuming that heat does not leave the plastic zone during fracture). Local ductility in the crack path may be expected since deformation and fracture would occur in material at an elevated local temperature. This effect would not be expected during slower fracture toughness testing (thermal conductivity is too high) and may hence explain the discrepancy between the K_{IC} and Charpy cryogenic toughness data for an Fe-8Ni alloy steel.[55]

The high solubility of substitutional and interstitial atoms in austenite suggests that the austenite may serve to enhance toughness by acting as a sink for deleterious elements. However, the high diffusivities of the light interstitials would indicate that a shorter final 600°C tempering treatment would be adequate to clean the martensitic microstructure. Hard chemical analysis data is clearly needed to test the

feasibility of this role of austenite as a "scavenger".

It is not necessary that the beneficial impact toughness effect of austenite occurs simultaneously with the $\gamma \rightarrow \alpha'$ transformation. If we presume that the deep transformation of austenite measured in this study indicates that the $\gamma \rightarrow \alpha'$ transformation precedes the crack tip, we may consider the beneficial effect in terms of the α' transformation product. If the reverted austenite transforms under stain to a ductile product, the new phase could quite conceivably promote local ductility in the path of the fracture crack. The untwinned, dislocated martensite observed by Syn [9] near the fracture surface of Fe-9Ni steel may also provide the ductility enhancement attributed to austenite in Fe-6Ni steel. Consideration of the behavior of the α' transformation product during crack propagation may be necessary in conjunction with all explanations of the low DBTT of tempered Fe-Ni cryogenic steels.

Uncovering the relationship between reverted austenite and the low DBTT of two-phase tempered Fe-Ni cryogenic steels is not a straightforward procedure. "Post-mortem" studies of fracture surfaces must rely on circumstantial evidence for their conclusions. Reasonable models can be experimentally tested and perhaps eliminated, but it is always necessary to allow for unforeseen explanations. For instance, although no evident microstructural changes in the martensite are brought about by the final tempering, the importance of such changes cannot be disregarded. These changes may only be subtle ones, but in steels nature can work in subtle ways.

REFERENCES

1. T. Ōoka, H. Mimura, S. Yano, K. Sugino and T. Toisumi, JJIM 30, 442 (1966).
2. Japanese Patent Publication No. 46-13498 (1971).
3. U. S. Patent No. 3619302 (9/11/72).
4. S. Nagashima, T. Ōoka, S. Sekino, H. Mimura, T. Fujishima, S. Yano and H. Sakurai, Trans. ISIJ 11, 402 (1971).
5. S. Yano, H. Sakurai, H. Mimura, N. Wakita, T. Ozawa and K. Aoki, Trans. ISIJ 13, 133 (1973).
6. K. Kim and L. Schwartz, Mat. Sci. and Eng., in press.
7. H. Haga, Trans. ISIJ 13, 141 (1973).
8. S. K. Hwang, S. Jin and J. W. Morris, Jr., Met. Trans. 6A, 2015 (1975).
9. C. K. Syn, B. Fultz and J. W. Morris, in press.
10. B. Fultz, unpublished results (1977).
11. G. Thomas, Met. Trans. 9A, 439 (1978).
12. B. Fultz and J. W. Morris, Jr., Rev. Sci. Instr., in press.
13. K. Miller, Trans. ASM 57, 892 (1964).
14. R. Mössbauer, Naturwissenschaften 45, 538 (1958).
15. H. Frauenfelder, The Mössbauer Effect (W. A. Benjamin, Inc., New York, 1962).
16. H. J. Lipkin, Ann. Phys. 9, 332 (1960).
17. R. L. Cohen, Applications of Mössbauer Spectroscopy (Academic Press, New York, 1976) Volume I.
18. C. Kittel, Quantum Theory of Solids, (J. Wiley, 1963) Chap. 20.
19. M. Graham, D. Mitchell and J. Phillips, N. Instr. and Methods 141, 131 (1977).
20. R. Cohen and G. Wertheim, Methods of Experimental Physics, (R. Coleman and L. Marton eds. Academic Press, New York, 1974) Volume 11, 307.

21. J. Spijkerman, NBS Technical Note 541 (1971).

22. K. Swanson and J. Spijkerman, Jour. Appl. Physics 41, 3155 (1970).

23. S. Marguiles and J. Ehrman, Nuclear Instr. and Methods 12, 131 (1961).

24. E. Daniel in Proc. Fermi School 1966, (W. Marshall ed., Academic Press, 1967), 386.

25. M. Collins and G. Low, Proc. Phys. Soc. London 86, 535 (1965).

26. I. Campbell, Proc. Phys. Soc. London 89, 71 (1966).

27. D. Shirley and G. Westenbarger, Phys. Rev. 138, A170 (1965).

28. D. Shirley, S. Rosenblum and E. Matthias, Phys. Rev. 170, 363 (1968).

29. G. Low, Jour. Appl. Phys. 39, 1174 (1968).

30. G. Wertheim, V. Jaccarino, J. Wernick and D. Buchanan, Phys. Rev. Lett. 12, 24 (1964).

31. A. Asano, Ph.D. Thesis, Northwestern University (1974).

32. T. Cranshaw, C. Johnson, M. Ridout and G. Murray, Physics Lett. 21, 481 (1966).

33. T. Cranshaw, Jour. Phys. F 2, 615 (1972).

34. I. Vincze and I. Campbell, Jour. Phys. F 3, 647 (1973).

35. B. Fultz, unpublished results 1978.

36. R. Tahara, Y. Nakamura, M. Inagaki and Y. Iwama, Phys. Stat. Solidi 41, 451 (1977).

37. C. Johnson, M. Ridout, T. Cranshaw and P. Madsen, Phys. Rev. Lett. 6, 450 (1961).

38. L. Walker, G. Wertheim and V. Jaccarino, Phys. Rev. Lett. 6, 98 (1961).

39. B. Window and G. Longworth, Jour. Phys. F 1, 718 (1971).

40. H. Frauenfelder, D. Nagle, R. Taylor, D. Cochran and W. Visscher, Phys. Rev. 126, 1065 (1962).

41. R. Nussbaum and R. Housley, Nucl. Phys. 68, 145 (1965).

42. H. Marcus, L. Schwartz and M. Fine, Trans. ASM 59, 468 (1966).

43. B. Christ and P. Giles, Trans AIME, 242, 1915 (1968).

44. L. Schwartz, Applications of Mössbauer Spectroscopy,(Academic Press, New York, 1976) Volume I, Chap. 2, R. Cohen ed.

45. N. Abe and L. Schwartz, Mater. Sci. and Eng. 14, 239 (1974).

46. J. de Launay, Solid State Physics, (F. Seitz and D. Turnbull eds., Academic Press, New York, 1956), Volume 2.

47. Y. Tanji, Jour. Phys. Soc. Japan 30, 133 (1971).

48. L. Schwartz and K. Kim, Met. Trans. 7A, 1565 (1976).

49. M. Varma and R. Hoffman, Jour. Appl. Phys. 42, 1727 (1971).

50. J. Pearson, Phys. Rev. 138, A213 (1965).

51. J. Terrell and J. Spijkerman, Appl. Physics Lett. 13, 11 (1968).

52. G. Simmons and H. Leidheiser, Jr., Applications of Mössbauer Spectroscopy, (Academic Press, New York, 1976) Volume I, R. Cohen ed.

53. B. Jain, A. Singh, K. Chandra and I. Saraswat, J. Jour. Appl. Phys. 16, 2121 (1977).

54. W. Leslie and R. Miller, Trans. ASM 57, 972 (1964).

55. S. Jin, S. K. Hwang and J. W. Morris, Jr., Met. Trans. 6A, 1721 (1975).

Table I: Identified Phases in Fe-6Ni Steel

	Martensite		Austenite	Rust	
Phase	α-Fe		γ-Fe	β-FeOOH	
Peaks Within ±2.0 mm/sec Scan	Two hyperfine split		one	two quadrupole split	
*Peak Centers	22.5	48.9	37.1	25	35
*Full Width at Half Maximum	4.8	4.4	6.1	7	7
Splitting of Peaks (mm/sec)	1.65		-	0.62	

*Lorentzian parameters in data channels. 1 data channel = .0625 mm/sec for ±2.0 mm/sec scan.

Table II: Polishing Procedure

Depth	Solution	Time
0.01 cm removal	60 drops HF in 100 ml 30% H_2O_2	90 sec
0.1 cm removal	10% HF - 27% H_2O_2 - 63% H_2O	7 min. followed by 0.01 cm procedure

FIGURE CAPTIONS

FIG. 1. Heat treatment and composition.

FIG. 2. Constrained-fatigue-notched specimen geometry.

FIG. 3. The Mössbauer Spectrometer.

FIG. 4. Spectrometer Timing Diagram.

FIG. 5. Data counters and control (top); printer interface logic (bottom).

FIG. 6. Cosine Broadening Functions (0.60 cm dia. source; 1.43 cm dia. detector). Percent velocity decrease is on the lower x-axis, y-axis is the probability of the velocity error.

FIG. 7. Pure Fe Spectra. Note the excellent fit to M3 by the Lorentzian function $L(x) = [1 + (2x/3.9 - 48.9)^2]^{-1}$ (where x ≡ data channel number) which gives a FWHM = 0.24 mm/sec.

Notation: M1 (+1/2 +3/2) M2 (+1/2 +1/2)
M3 (+1/2 -1/2) M4 (-1/2 +1/2)
M5 (-1/2 -1/2) M6 (-1/2 -3/2)

for absorptions with (ground excited) spin alignments.

FIG. 8. Fe-6Ni spectra.

FIG. 9. Comparison of M3 and M4 peaks.

FIG. 10. 14 neighbor shell model fits to M6 peaks. 10a) component Lorentzian FWHM = 0.24 mm/sec; 10b) component Lorentzian FWHM = 0.31 mm/sec. The statistically significant bump in the experimental points around channels 36-43 is due to Fe atoms with one Mn atom in their 1st n.n. shell (see also Fig. 8). The shift is compatible with data from Refs. 28 and 32 for the Mn content of our alloy.

FIG. 11. Difference between the 14 neighbor shell model peaks and their best-fitting single Lorentzian curve

j ≡ FWHM for component curves in the linear hyperfine perturbation model.

J ≡ FWHM of best fitting single Lorentzian.

FIG. 12. M3 peak predicted by 14 neighbor shell model with parameters giving the best data fit. A good approximation to this lineshape is provided by a single Lorentzian function.

FIG. 13. Idealized spectral analysis procedure.

FIG. 14. 0.01 cm polished 77°K Charpy fracture surface showing 0.0 ± 0.5% austenite after stripping.

FIG. 15. Reverted austenite in a 0.1 cm polished undeformed surface.

FIG. 16. Austenite depth profile (austenite concentration data from depths $\lesssim$10μm is possible by counting backscattered 14.4 keV γ-rays. Experimental difficulties rendered this data unusable.

FIG. 17. Depth of transformation as a function of absorbed impact energy.

FIG. 18. The martensite transformation as a function of depth and impact energy.

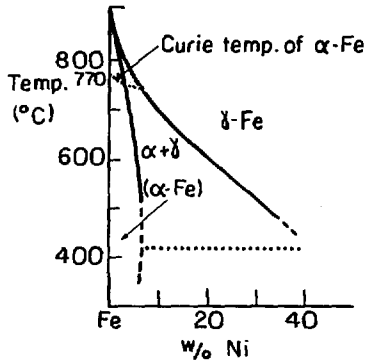

QLT Treatment

Q = 800°C (1 hr) WQ

L = 670°C (1 hr) WQ

T = 600°C (1 hr) WQ

Composition, w/o

Ni	Mn	Mo	Cr	Si	C	P	S	Fe
5.75	0.93	0.5	0.16	0.19	0.06	0.06	0.05	Bal.

XBL 785-5031

FIG. 1

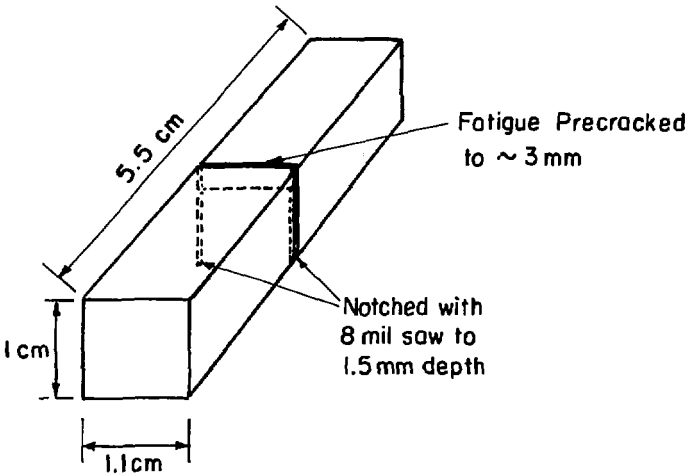

XBL 785-5030

FIG. 2

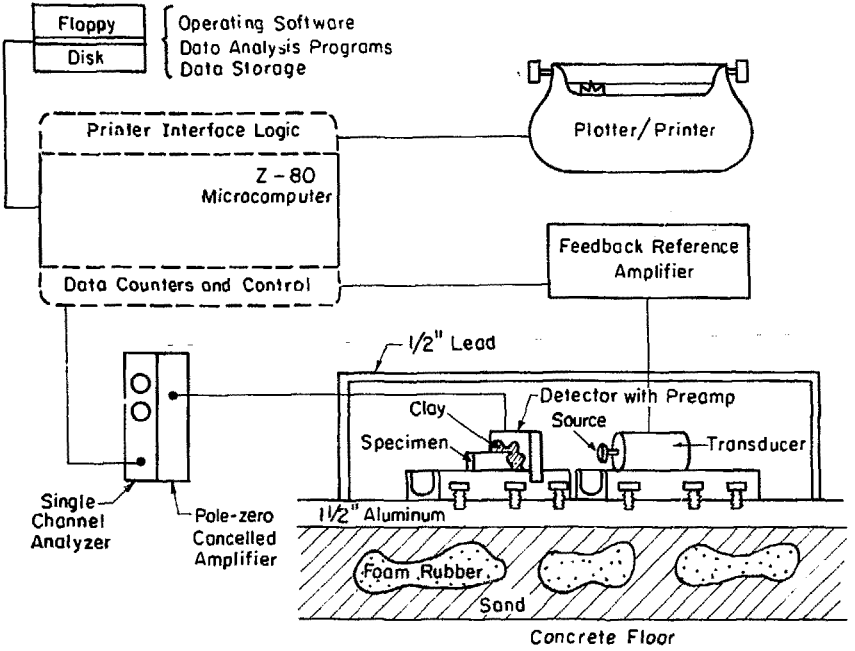

XBL 785-5036

FIG. 3

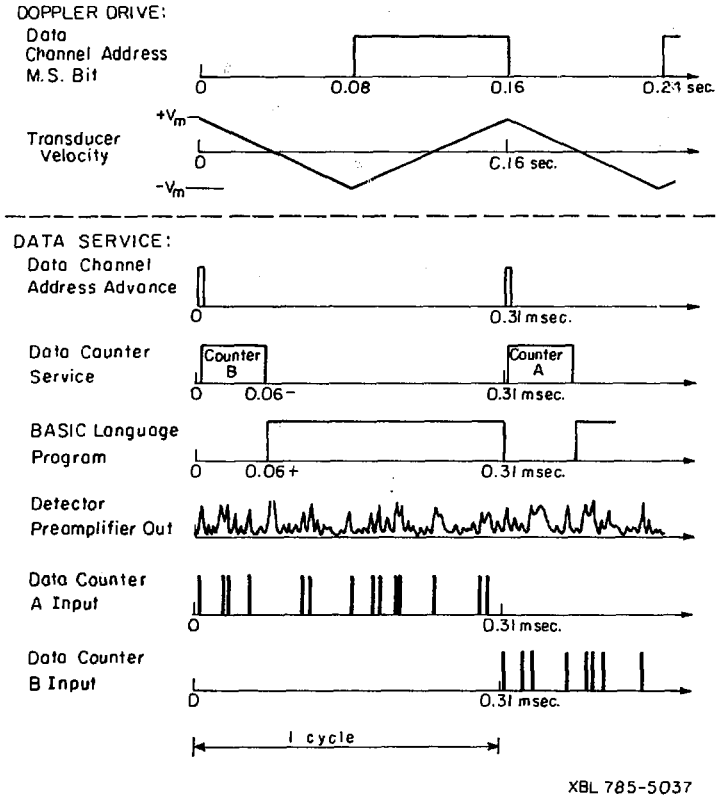

XBL 785-5037

FIG. 4

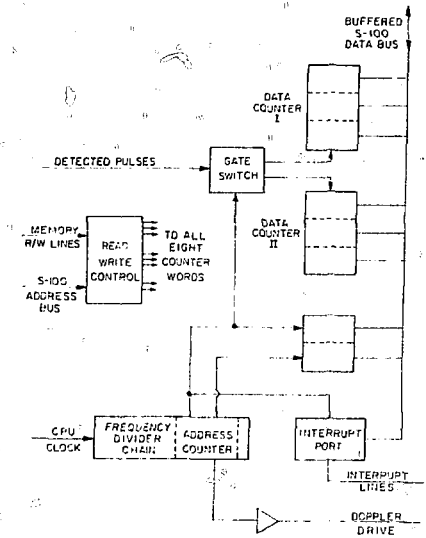
BUFFERED
S-100
DATA BUS
DATA
COUNTER
I
DETECTED PULSES
GATE
SWITCH
MEMORY
R/W LINES
READ
WRITE
CONTROL
TO ALL
EIGHT
COUNTER
WORDS
S-100
ADDRESS
BUS
DATA
COUNTER
II
CPU
CLOCK
FREQUENCY
DIVIDER
CHAIN
ADDRESS
COUNTER
INTERRUPT
PORT
INTERRUPT
LINES
DOPPLER
DRIVE

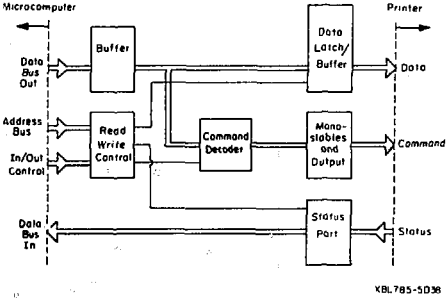
Microcomputer
Printer
Buffer
Data
Bus
Out
Data
Latch/
Buffer
Data
Address
Bus
Read
Write
Control
Command
Decoder
Mono-
stables
and
Output
Command
In/Out
Control
Status
Port
Status
Data
Bus
In
XBL785-5038

FIG. 5

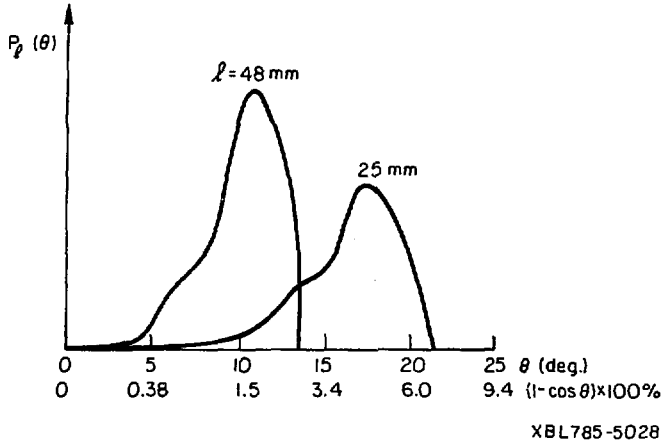
P_ℓ (θ)
ℓ = 48 mm
25 mm
0 5 10 15 20 25 θ (deg.)
0 0.38 1.5 3.4 6.0 9.4 (1-cos θ)×100%
XBL785-5028

FIG. 6

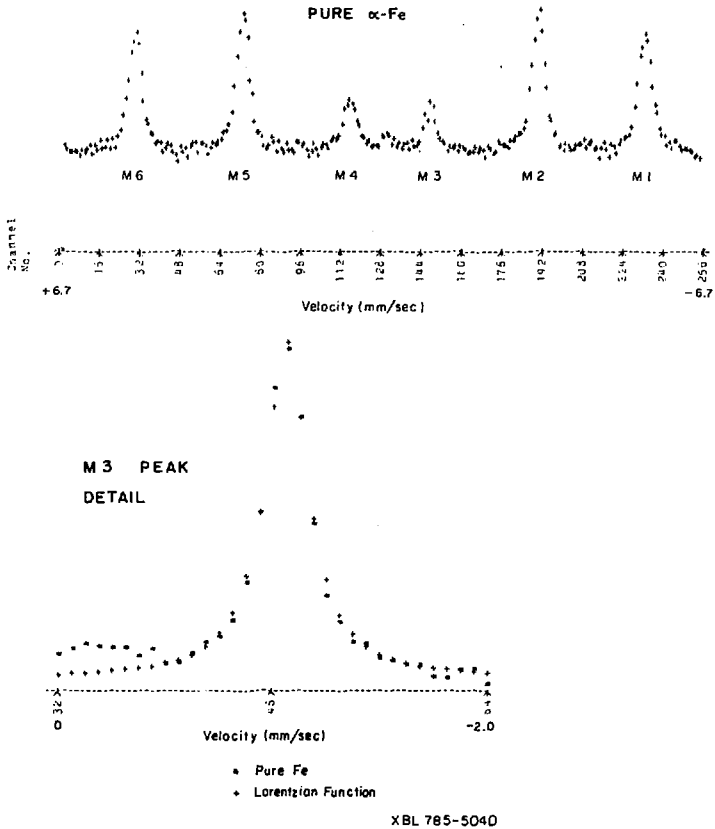
PURE α-Fe
M6
M5
M4
M3
M2
M1
Channel No.
+6.7
-6.7
Velocity (mm/sec)
M3 PEAK
DETAIL
0
-2.0
Velocity (mm/sec)
Pure Fe
Lorentzian Function
XBL 785-5040

FIG. 7

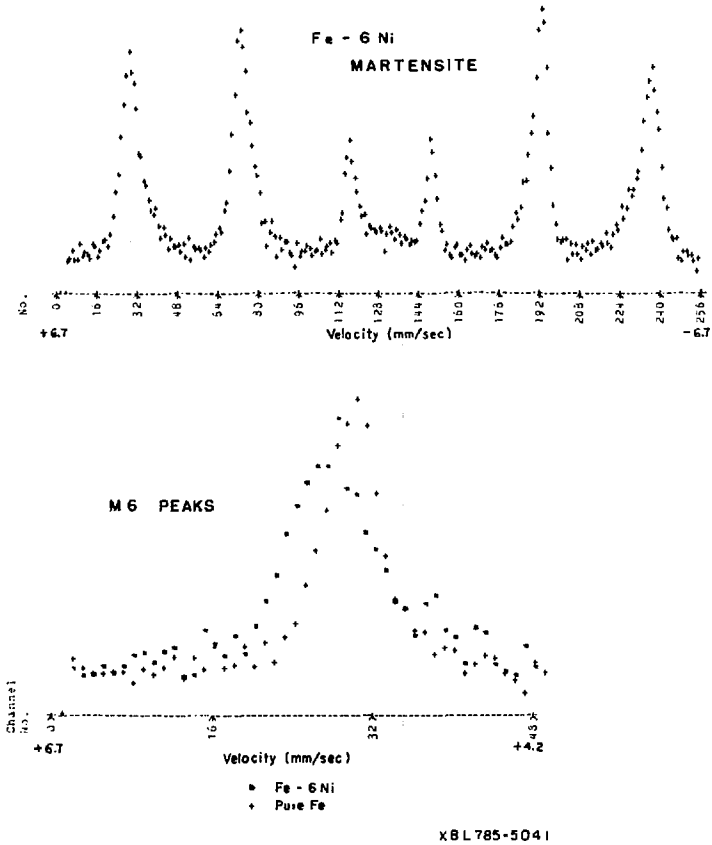
Fe - 6 Ni
MARTENSITE
No.
0
16
32
48
64
80
96
112
128
144
160
176
192
208
224
240
256
+6.7
Velocity (mm/sec)
-6.7
M 6 PEAKS
Channel No.
0
16
32
48
+6.7
Velocity (mm/sec)
+4.2
Fe - 6 Ni
Pure Fe
XBL785-5041

FIG. 8

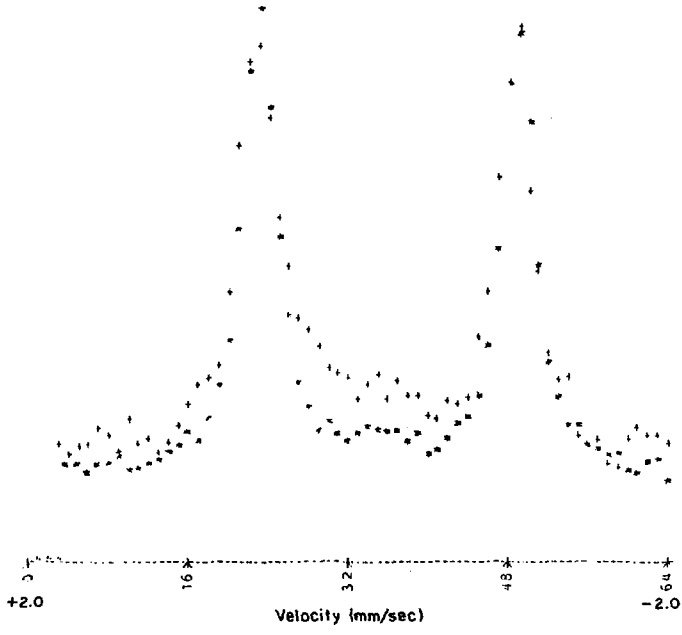

+ Fe - 6 Ni (α-Fe, β-FeOOH)

* Fe foil (α-Fe)

XBL 785-5048

FIG. 9

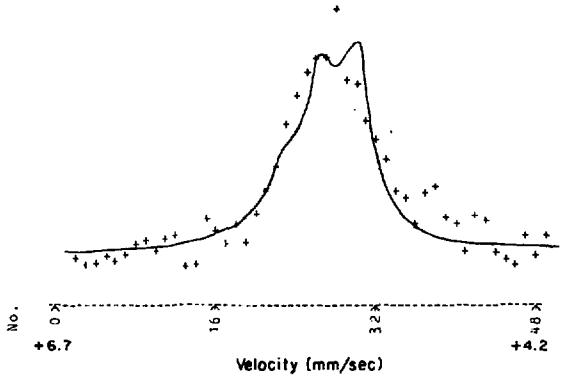

+ Fe - 6 Ni Data

(A)

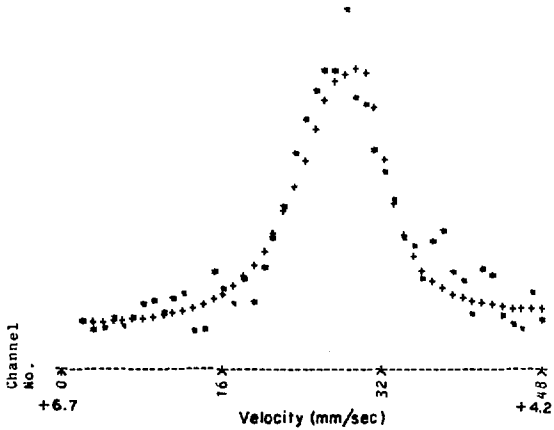

* Fe-6Ni Data

(B)

XBL 785-5044

FIG. 10

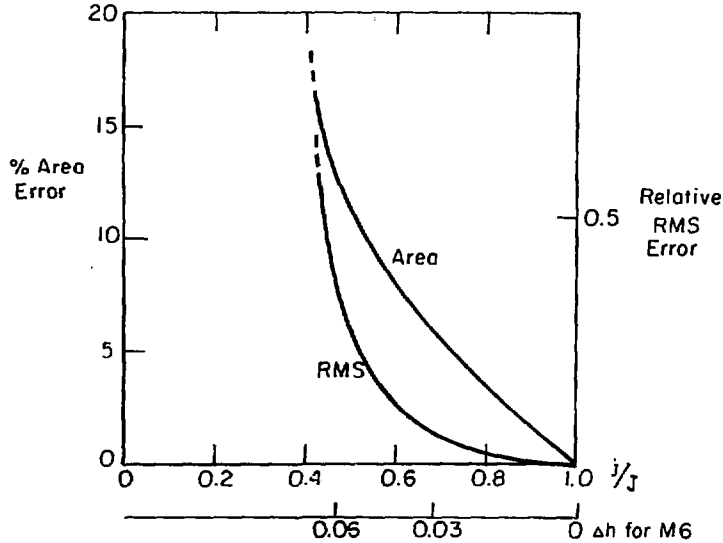

XBL785-5029

FIG. 11

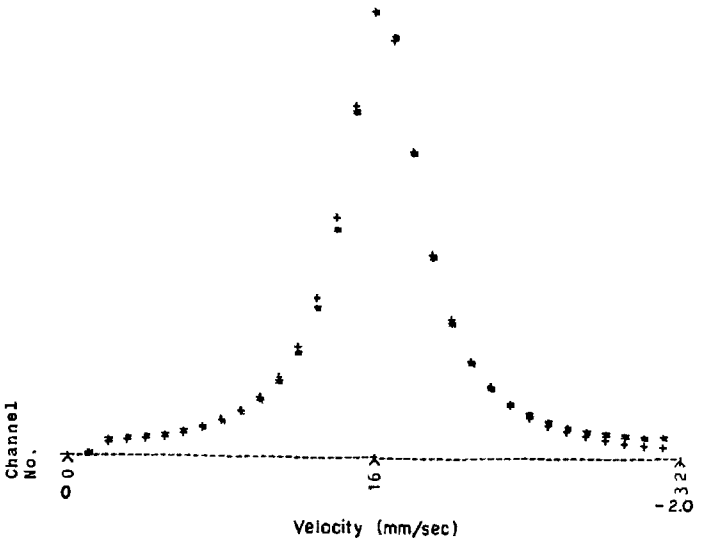

* 14 Lorentzians
\+ Single Lorentzian

FIG. 12

XBL785-5039

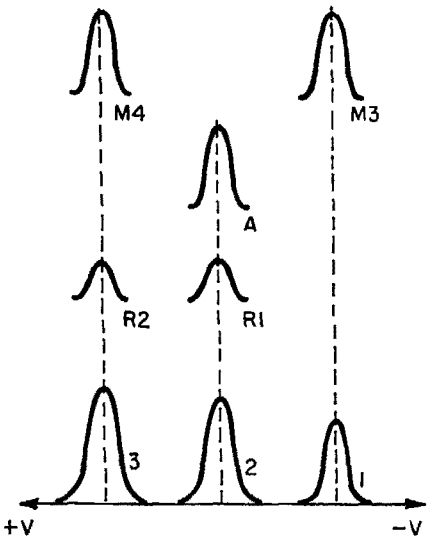

Phase	Constraint
α - Fe	I(M3)=I(M4)
γ - Fe	
β - FeOOH	I(R1)=I(R2)
Sum of Above	I(1)=I(M3) I(2)=I(A)+I(R1) I(3)=I(M4)+I(R2)

Notation: I(X) = Intensity of Peak X (area)

FIG. 13

XBL 785-5032

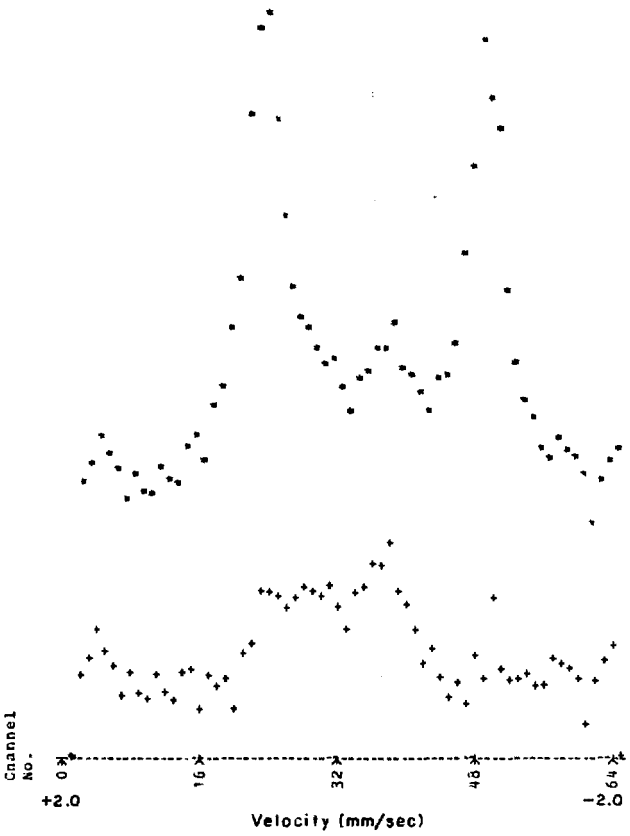

XBL 785-5046

FIG. 14

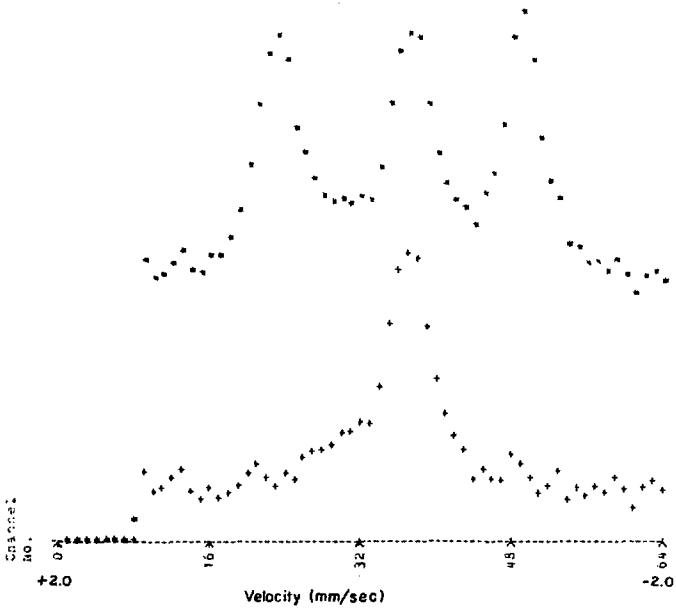

* Fe-6 Ni undeformed surface
+ Stripped to show γ-Fe and β-FeOOH

XBL 785-5047

FIG. 15

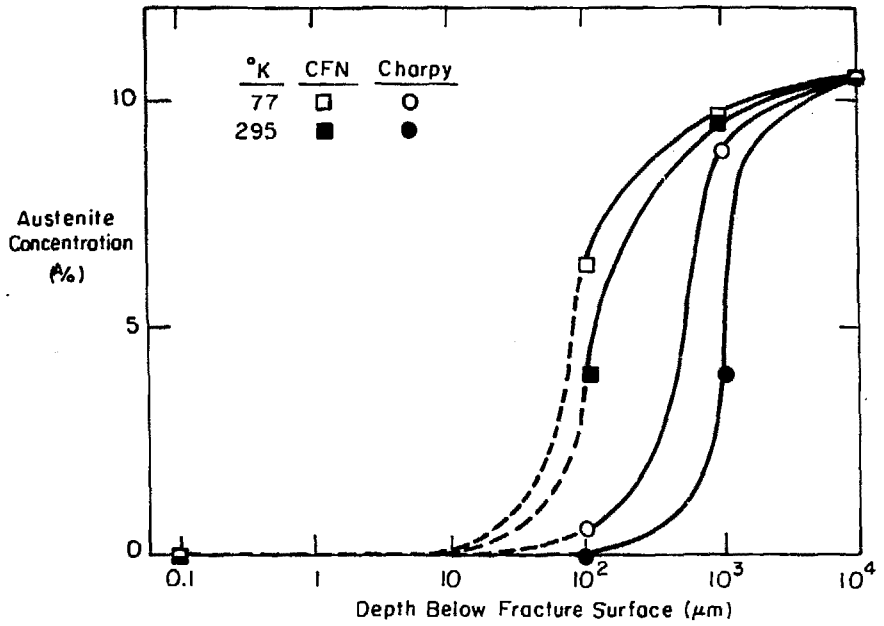

FIG. 16

XBL 785-5033

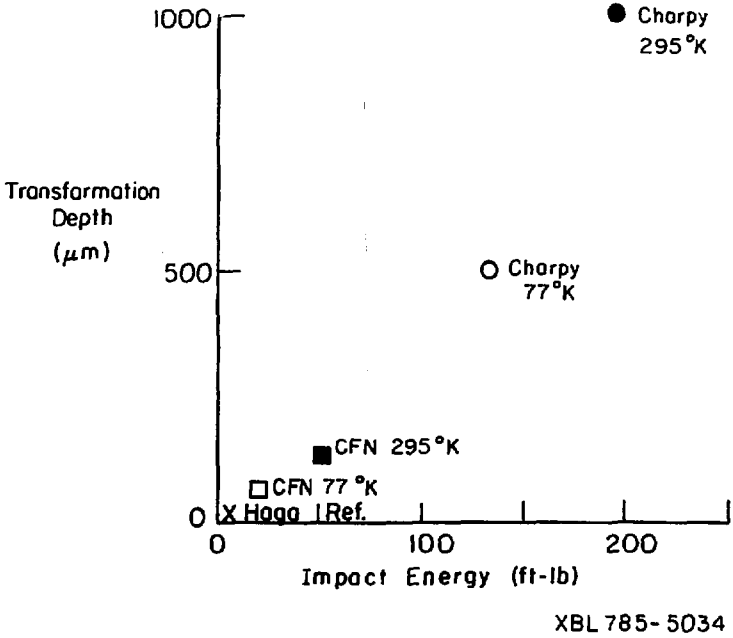
1000
500
0
Transformation
Depth
(μm)
Charpy
295°K
Charpy
77°K
CFN 295°K
CFN 77°K
X Haga Ref.
0
100
200
Impact Energy (ft-lb)
XBL 785-5034

FIG. 17

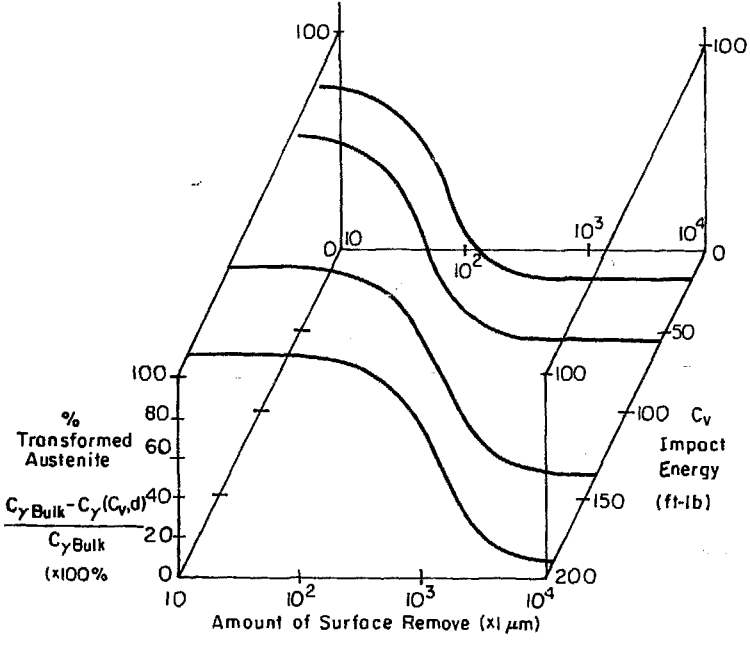

FIG. 18

XBL 785 - 5035